This is an open access article published under a Creative Commons Attribution (CC-BY) License, which permits unrestricted use, distribution and reproduction in any medium, provided the author and source are cited.

ACS AUTHORCHOICE

THE JOURNAL OF PHYSICAL CHEMISTRY A

pubs.acs.org/JPCA Article

Incorporating Solution-Processed Mesoporous WO_3 as an Interfacial Cathode Buffer Layer for Photovoltaic Applications

Anurag Roy, Shubhranshu Bhandari, Aritra Ghosh,* Senthilarasu Sundaram, and Tapas K. Mallick

Cite This: *J. Phys. Chem. A* 2020, 124, 5709–5719 Read Online

ACCESS | Metrics & More | Article Recommendations | Supporting Information

ABSTRACT: Dextran-templating hydrothermal synthesis of monoclinic WO_3 exhibits excellent specific surface area of ~110 m^2/g and a monomodal pore distribution with an average pore diameter of ~20 nm. Dextran plays a crucial role in generating porosity on WO_3. The role of supporting dextran has been investigated and found to be crucial to tune the surface area, porosity, and morphology. The photoluminescence and X-ray photoelectron spectroscopy studies reveal the existence of oxygen vacancies in substoichiometric WO_3, which creates localized defect states in WO_3 as synthesized through this templating method. The highly mesoporous WO_3 has been further explored as an interfacial cathode buffer layer (CBL) in dye-sensitized solar cells (DSSCs) and perovskite solar cells (PSCs). A significantly enhanced photoconversion efficiency has boosted up the performance of the counter electrode used in traditional DSSC (as platinum) and PSC (as carbon) devices by ~48 and ~29%, respectively. The electrochemical impedance and incident photon to current conversion efficiency (IPCE) studies were also analyzed in order to understand the catalytic behavior of the WO_3 interfacial CBL for both DSSCs and PSCs, respectively. The much higher surface area of WO_3 enables rapid electron hopping mechanism, which further benefits for higher electron mobility, resulting in higher short circuit current. Through this study, we were able to unequivocally establish the importance of buffer layer incorporation, which can further help to integrate the DSSC and PSC devices toward more stable, reliable, and enhanced efficiency-generating devices. In spite of this, using WO_3 constitutes an important step toward the efficiency improvement of the devices for futuristic photoelectrochromic or self-powered switchable glazing for low-energy adaptive building integration.

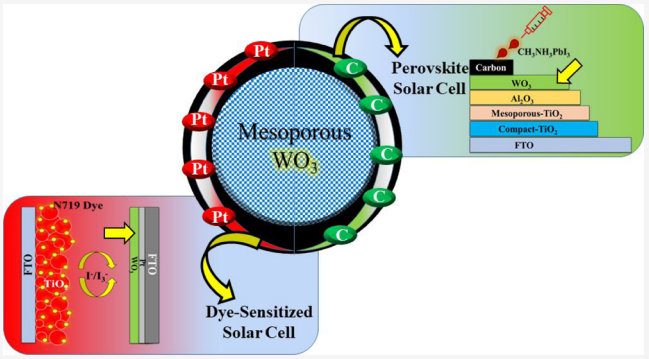

INTRODUCTION

In the recent past, there has been a great impetus to develop and design functional materials for energy-harvesting applications in the field of dye-sensitized solar cells (DSSCs) and perovskite solar cells (PSCs).[1−4] While researching new ways to increase the efficiency of utilizing solar energy, the technology is constantly being developed into new and better-advanced products. DSSCs stand out as one of the front runners in view of the basic novelty of the concept derived from nature's principles, which allows facile and cost-effective processing alternatives.[5,6] PSCs are thus considered as an advancement over DSSCs, where the photoanode thickness is reduced to a few microns and the dye is replaced by a superior light-absorbing organometal halide perovskite supported by a hole-transporting layer, which can be deposited directly over this cell architecture.[7] Among the research and development versatility of the third-generation solar cell photovoltaic (PV) area, PSCs are the best technology developed during the last few years that promise a cheaper and more efficient alternative to the existing technologies for converting light to electric power.[8,9] Implementation of various structures and fabrication strategies such as nanostructured materials (core−shell, mesoporous, one-dimensional, composite),[10] advanced light-harvesting materials (quantum dots, NIR sensitizers),[11,12] solid-state electrolytes,[13] elimination of hole-transport materials (HTM),[14] flexible substrates,[15] scattering layers,[16] up-conversion materials,[17] and encapsulation methods,[18] therefore, is envisaged as a potential effort to achieve prolonged stability and high efficiency in DSSC and PSC devices. The motive of all these strategies is efficient collection and extraction of charges. Additionally, introducing a buffer layer can provide enormous support, depending on where it has been used in the device. In general, a cathode buffer layer (CBL) excels as a supportive or optional layer for the cathode or back electrode material, which protects the cell from air and moisture and hence induces enhanced perform-

Received: April 1, 2020
Revised: June 10, 2020
Published: June 11, 2020

Downloaded via UNIV OF EXETER on August 20, 2020 at 12:47:15 (UTC).
See https://pubs.acs.org/sharingguidelines for options on how to legitimately share published articles.

ance and stability of the device.[19] Besides, as a protective layer, CBL employment further catalyzes the electron−hole separation too. Similarly, the primary function of an anode buffer layer in a heterojunction is to form a junction with the absorber layer while admitting a maximum amount of light to the junction region and absorber layer.[20]

Several commonly used CBLs were first established for organic light-emitting diodes and then transferred to organic solar cells (OSCs).[21] Traditionally, CBL imparts as an inert, solution-processable substitute of calcium oxide; it is a hot spot in the field of OSCs and has achieved a significant efficiency of 9.2% in this field.[22] In this regard, CBL can no more be considered as an optional layer but is an essential layer for achieving maximum performance in OSCs. In OSCs, there are also several studies on the application of fullerene derivatives as buffer layers. Liang et al. (2015) showed an enhanced efficiency of 15.44% using the fullerene buffer layer for $CH_3NH_3PbI_3$-based PSCs,[23] whereas using TiO_2 buffer layer, there is a significant and exceeds the enhancements of ∼42% efficiency has been achieved by Lungu et al. (2019), for the DSSC device.[24] The effective hole-blocking role of the TiO_x layer in the poly(3-hexylthiophene) (P3HT) and phenyl-C_{61}-butyric acid methyl ester ($PC_{61}BM$) system was investigated, and significant improvements in the efficiency were obtained: from 2.3 to 5.0% and from 1.4 to 4.0%, respectively.[25,26] The implementation of CBL for DSSC- or PSC-based devices has been overlooked because of other predominatant alternative strategies, as a result, realization of CBL's performance further opens up ample scope for further research. Lithium fluoride (LiF)-based CBL in PSCs has been demonstrated to enhance the device performance through the formation of an interfacial dipole at the cathode interface.[27] However, ZnO is the most extensively investigated one for CBLs among the metal oxide-based CBL for the inverted PSCs, mainly because of its suitable energy levels, high electron mobility, good transparency, environmental stability, and low cost.[28] Recently, Rajbhandari et al. (2020) reported the effect of three different oxide CBLs, such as Al_2O_3, ZnO, and TiO_2, deposited by atomic layer deposition method in PSCs.[29] Tran et al. (2016) demonstrated about the implementation of SnO_2 nanoparticles as a CBL for an inverted OSC, which revealed excellent long-term device stability, and the photoconversion efficiency (PCE) was retained as ∼95% (2.89%) of its initial value after 10 weeks in ambient air.[30] Using MoO_x as a CBL could also be able to improve the efficiency from 1.3 to 5.52% for an all-inorganic $CsPbIBr_2$-based PSC.[31] Aside from rapid progress in the field of PSCs, originated from a variety of device configurations, metal-oxide buffer layer implementation is still a less-explored research interest.

Along with this, mesoporous characteristics in the devices stand out as a skillful technique, leading to heightened efficiency because of greater availability of active sites in the substrate. The effect of mesoporosity has been demonstrated not only for the metal oxide scaffold but also for the counter electrode.[32] The redox functionality of the devices is intimately related to the dynamics of charge transfer (CT)/electron transport across the mesoporous layer, which, in turn, is strongly influenced by the nanostructured morphology of the film.[33] In this work, a biocompatible, water-soluble dextran has been employed as a soft templating agent for porosity improvement in the WO_3 structure. Dextran has been found to be a promising soft templating agent for metallic sponge and high-surface-area developing and structure-directing synthesis.

WO_3 is an extensively studied potential candidate for PV devices.[34,35] With a view to enhance the PCE, research focused on the exploration of WO_3 as a photoanode material retarding the efficiency because of high band gap and less electron mobility than that of DSSCs based on the other semiconducting metal oxides, such as TiO_2 and ZnO, without employing any surface modification.[36] On the other hand, efforts to replace organic polymers with WO_3, as a hole injection layer (HTL) in PV cells leads to exhibit higher device performance, which are currently receiving increased attention. However, the methods such as sputtering, thermal evaporation, and pulsed laser deposition, involve depositing the WO_3 layer, which is incompatible with a low-cost and solution-processed layer for future scalable manufacturing.

In this study, our target is to integrate the mesoporous WO_3 as an n-type metal oxide-based CBL for DSSC and PSC devices. To achieve a high surface area and considerable mesoporosity features of WO_3, a dextran-templating hydrothermal synthesis process has been attempted. The synthesized WO_3 has been further characterized by various physiochemical techniques and finally introduced as a CBL for DSSC and PSC devices. Further, our subsequent agenda is to imply this WO_3-based PV devices for electrochromic (EC) switchable glazing applications. The glazing has the ability to tune its color in the presence of applied direct current electric power. By changing the transparency, an EC switchable window attenuates glare and undesired solar gains, which provides improved indoor comfort.

MATERIALS AND METHODS

Materials. Sodium tungstate ($Na_2WO_4{\cdot}2H_2O$), HNO_3, and HCl were purchased from Merck, and dextran (molecular weight ca. 75,000) was acquired from Alfa Aesar, Ward Hill, MA. Isopropanol and propylene glycol were purchased from Sigma-Aldrich, UK. All the chemicals were used without any further purification.

Synthesis of Porous WO_3. Hierarchically porous WO_3 assemblies were synthesized by the hydrothermal method. In a typical experiment, 1.98 g of sodium tungstate ($Na_2WO_4{\cdot}2H_2O$) was first dissolved in 40 mL of distilled water, and then, 1.5 mL of HNO_3 aqueous solution was added dropwise into the above solution under constant stirring to prepare tungstic acid H_2WO_4. H_2O (8 mol L^{-1}, pH 2). To this solution, 10 g of dextran has been added to further prepare an aqueous viscous solution to control the growth, leading to porous textures at room temperature. To allow the dextran-formatting network throughout the aqueous solution of sodium tungstate for texture formation and further porosity development, the entire viscous solution was further kept completely under an undisturbed condition overnight. After this, the solution was transferred into a 50 mL Teflon-lined autoclave for the hydrothermal treatment at 160 °C for 24 h. The yellowish product as obtained from the hydrothermal reaction was accordingly centrifuged at 10,000 rpm and successively washed with 0.1 M HCl to neutralize the solution pH to 7. Besides, HCl treatment further helps to remove any unreacted Na^+ ion also. The collected product was dried under an infrared lamp at ∼80 °C for 12 h followed by calcination at 300 °C for a period of 1 h to get the final product. The same synthesis process has been carried out without dextran to understand the role of dextran in controlling the morphology and porosity. The overall synthesis scheme has been represented in Figure 1. In this synthesis, dextran excels as a porosity developer and

https://dx.doi.org/10.1021/acs.jpca.0c02912
J. Phys. Chem. A 2020, 124, 5709−5719

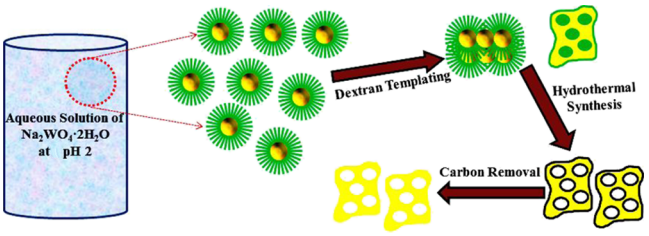

Figure 1. Schematic representation of the formation of hierarchically porous WO_3 assembly by the hydrothermal reaction.

morphology-texturing agent, which is required to obtain a high surface area of WO_3. It is anticipated that the dextran-formatting network behaves like a mould where the WO_3 precursor was attached. During the hydrothermal treatment, the removal of dextran further leads to the creation of pores on the particles.[37]

Fabrication of DSSCs. Pieces with an area of 2 × 2 cm^2 of transparent conducting oxide [fluorine-doped tin oxide (FTO)] glass substrates were first ultrasonicated in deionized water and ethanol. Next, they were subjected to surface cleaning by using an UV-Ozone cleaner (Ossila UV Ozone Cleaner, UK) for 15 min to remove any dirt, patches on the surface of the FTO glasses. Next, a layer of transparent TiO_2 paste (18NR-T, GreatCell Solar) was allowed for screen printing (120 T mesh/inch) on the UV-ozone-treated FTO glasses and dried for 6 min on a hotplate at 125 °C. After this, another layer of a similar transparent TiO_2 was deposited by the same method. The screen-printed active area of the working electrode was selected as 0.28 cm^2. Then, a final layer of opaque TiO_2 paste (18NR-O, GreatCell Solar) was printed, which provides an approximate thickness of 10−12 μm for the TiO_2 electrode. The prepared electrodes were heated on a hotplate at 450 °C for 30 min to allow the crystallization of the TiO_2 layer and to remove the binders available in the paste. After cooling down to 50 °C, the TiO_2 electrodes were immersed in a 0.1 mM ruthenium 535 bis-TBA (N719) dye from GreatCell Solar in a 1:1 acetonitrile and ethanol solution at room temperature for 24 h to assure complete uptake of sensitizer.[38] The Pt CE (Dyesol) was placed on a spin coating unit (SPIN 1200D, MIDAS System). A volume of 10 wt % (weight/volume) of a colloidal suspension of WO_3 was prepared in a 2:1 isopropanol and propylene glycol medium. A volume of 1 mL of prepared WO_3 colloidal solution was then spin-coated on the top of the FTO substrate at a speed of 3000 rpm for 30 s and dried at 200 °C for 30 min. Finally, the Platisol (T/SP, Solaronix ref. 41250) paste was drop-casted over the WO_3 film and further calcined at 450 °C for 10 min to deposit a layer of Pt. The similar process has also been followed for nonporous WO_3 layer deposition. The fabricated WO_3−Pt CE was further placed over the dye-sensitized photoanode, and a plastic spacer was kept in between these two electrodes. The prepared redox electrolyte of I^-/I_3^- was further infiltrated into the device and allowed for final testing.[37] A scheme of the WO_3 buffer layer-based DSSC device is given in Figure 2a.

Fabrication of PSCs. The PSC devices were fabricated as per our previous report.[35] However, for this case, 1 mL of the prepared WO_3 colloidal solution, as used for DSSC fabrication, was spin-coated at a speed of 3000 rpm for 30 s on the top of Al_2O_3 layer deposition and further heated at 200 °C for 30 min during the PSC fabrication. The similar process has been also

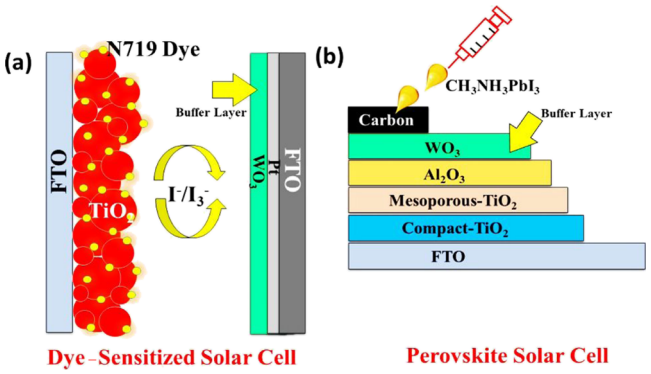

Figure 2. Schematic diagram of the WO_3 buffer layer in (a) DSSCs and (b) PSCs, respectively.

followed for nonporous WO_3 layer deposition as well. The mesoscopic carbon layer was finally screen-printed with the as-prepared carbon paste and sintered at 450 °C for 30 min. Finally, the perovskite precursor solution ($CH_3NH_3PbI_3$) with an appropriate amount was infiltrated by drop-casting via the top of the carbon counter electrode and further spin-coating at a speed of 1000 rpm for kept at 50 °C for 1 h and finally used for further studies. The active area of the working electrode was selected as 0.25 cm^2. A schematic configuration of the WO_3−carbon-based PSC is described in Figure 2b.

Materials Characterization. The structural properties of the as-prepared and calcined powders are characterized by using a Bruker D8 Advance X-ray diffractometer (Billerica, MA, USA). The morphology of the synthesized WO_3 was characterized using a high-resolution scanning electron microscope TESCAN VEGA3 SEM coupled with energy-dispersive spectroscopy (EDS; Oxford instrument elemental analysis) and a JEOL 2100 200 KV transmission electron microscope (TEM) providing a point resolution of 0.25 nm and a lattice resolution of 0.14 nm. The fluorescence spectrum was recorded at 22 ± 0.5 °C in 10 mm path length quartz cuvettes using a Quanta Master 400 unit (Horiba PTI, Canada) with a 150 W xenon lamp controlled by FelixGX spectroscopy software provided with the instrument. The X-ray photoelectron spectroscopy (XPS) measurements were carried out on a PHI 5000 Versa probe II scanning XPS microprobe (ULVAC-PHI, U.S.). The measurement was performed at room temperature at a base pressure higher than 6 × 10^{-10} mbar. All spectra were recorded with monochromatic Al Kα ($h\nu$ = 1486.6 eV) radiation with a total resolution of about 0.7 eV and a beam size of 100 μm. Nitrogen physisorption measurements of all the samples were carried out by using a Quantachrome (iQ3) instrument after evacuation at 150 °C for 4 h. The specific surface area was calculated by the Brunauer−Emmett−Teller (BET) method, whereas desorption cumulative pore volume and pore size distribution were calculated by the Barrett−Joyner−Halenda (BJH) method.

Device Testing. The photovoltaic measurements of both DSSC and PSC devices were performed under 1000 W/m^2 of light from a Wacom AAA continuous solar simulator (WXS-210S-20, AM1.5 G). The I−V characteristic of the devices was recorded using an EKO MP-160i I-V Tracer. Electrochemical impedance spectroscopy (EIS) measurements were carried out using an AUTOLAB frequency analyzer setup equipped with an AUTOLAB PGSTAT 10 and a Frequency Response Analyzer (FRA) Module. The measurements were performed under the same solar simulator conditions with a frequency

https://dx.doi.org/10.1021/acs.jpca.0c02912
J. Phys. Chem. A 2020, 124, 5709−5719

range from 0.1 Hz to 100 kHz. All the devices were measured at their corresponding open-circuit voltage. Incident photon to current efficiency (IPCE) was carried out using a Bentham PVE300 Photovoltaic EQE (IPCE) and IQE solution under 300−800 nm wavelength using a tungsten halogen lamp source.

RESULTS AND DISCUSSION

Structural, Optical, and Surface Area Analysis of WO_3. X-ray diffraction pattern, as shown in Figure 3, reveals

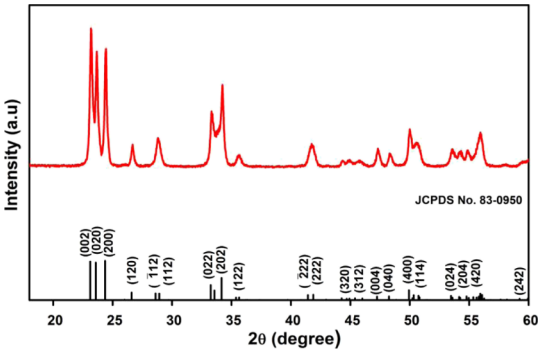

Figure 3. X-ray diffraction pattern of the synthesized monoclinic WO_3 sample.

the polycrystalline monoclinic WO_3 structure as it matches well with the reference diffraction pattern of WO_3 (JCPDS card number 83−0950). The main diffraction peaks at 23.1, 23.7, and 24.4° ascribed to Miller indices (002), (020), and (200), respectively, correspond to the monoclinic WO_3 phase. This also rationalizes the synthesized WO_3 free of orthorhombic WO_3 and $WO_3 \cdot 1/3H_2O$ phases showing that the products are pure phase. High and sharp peak intensities indicate an excellent crystallinity of the sample. It is interesting to mention here that the orthorhombic phase of WO_3 or $WO_3 \cdot 1/3H_2O$ is quite often to be obtained *via* the hydrothermal treatment of tungstic acid H_2WO_4. H_2O, although upon further heating >300 °C, all these metastable oxides lead to the stable monoclinic WO_3 phase.[39,40] Here, through this dextran-templating synthesis, the WO_3 attained the monoclinic phase directly.

In order to ascertain the effect of dextran addition on porosity improvement, the TEM investigation was performed with both the dextran-added and without dextran samples of WO_3, respectively. Figure 4a,b indicate the TEM bright-field images of WO_3 in the absence of dextran. It has been clearly observed that there are, as such, no porous characteristics formed on the WO_3 surface. Moreover, without dextran employment, it leads to form a densely populated large hierarchical structure, whereas the addition of dextran assists to render the porous nature throughout the surface of WO_3, as shown in the TEM bright-field images of Figure 4c,d at different magnifications. Besides, dextran addition influences to attain the morphology of WO_3 toward a separated hierarchical platelet-like structure. During the hydrothermal treatment, the chainlike structure of the dextran preferentially combines with the hydroxide nanocrystals of WO_3 anisotropically as building blocks thereby able to create patterned slits, which also facilitates the etching of the sites without the adsorption of dextran.[37] This may cause the pore formation of WO_3, allowing higher surface energy. In addition, Figure 4e shows the nitrogen adsorption−desorption isotherm of the WO_3 sample in the absence of dextran and appeared as type III isotherm. It exhibits a BET surface area of 30.28 $m^2\ g^{-1}$, involving no mesoporous characteristics, whereas the isotherm indicated mesoporous characteristic of the dextran-assisted WO_3 samples and appeared as type IV isotherm as reported in Figure 4f. The appearance of type H-3 hysteresis indicating a stacked-plane (slit)-like pore shape.[41] This exhibits comparatively a high surface area of 110.68 $m^2\ g^{-1}$. To the best of our knowledge,

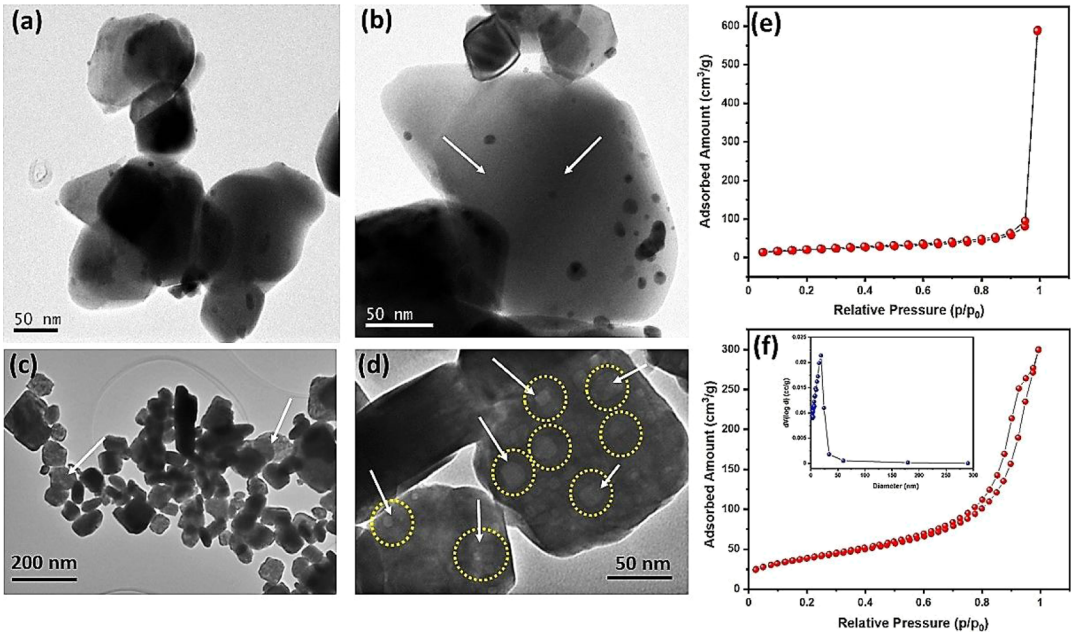

Figure 4. TEM bright-field images of (a,b) without dextran; (c,d) dextran-added WO_3 samples at different magnifications, respectively; nitrogen adsorption−desorption isotherm plot (e) in the absence of dextran and (f) dextran-added WO_3 samples (inset: corresponding pore size distribution plot), respectively.

https://dx.doi.org/10.1021/acs.jpca.0c02912
J. Phys. Chem. A 2020, 124, 5709−5719

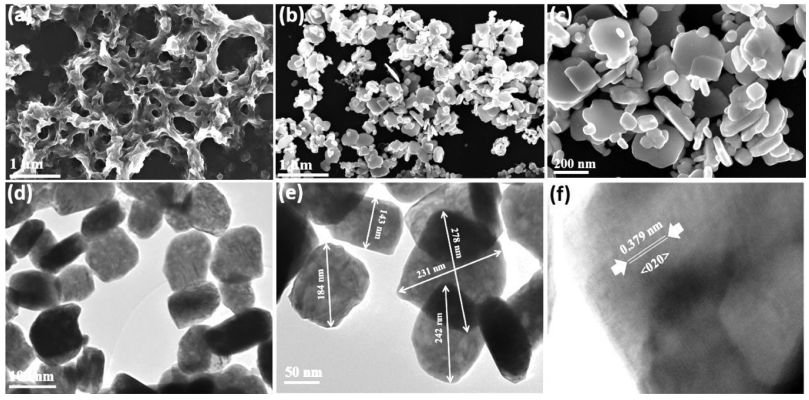

Figure 5. FESEM microstructural images of (a) the as-prepared sol, (b,c) mesoporous WO_3 at different magnifications, respectively; (d,e) TEM bright-field images of mesoporous WO_3 at different magnifications, respectively and (f) the corresponding HRTEM image.

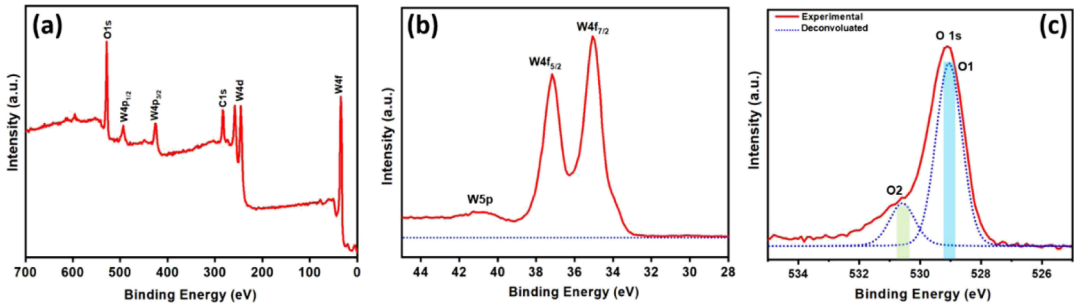

Figure 6. (a) XPS survey spectrum of the mesoporous WO_3 sample, (b) XPS of spin−orbit split peaks of W 4f, and (c) spectral decomposition of the O 1s spectrum results in two different types of oxygen environment denoted as the O1- and O2-fitted component in the WO_3.

the obtained surface area of this WO_3 is quite higher compared to the other similar reports of WO_3 as shown in Table S1.[42−51] The pore diameter was found to be about 3.7 nm using the BJH method adsorption method (Figure S2). This value was artifice (pseudo peak) calculated from the BJH computation method. Further, the pore diameter was found to be about 20.2 nm using the BJH desorption method, which was further supported by TEM investigation, as shown in Figure 4f (inset). The corresponding pore volume was found to be 0.46 cc g^{-1}. Again, stacked-plane pore geometry throughout the plate-like microstructural framework was fairly visible under a transmission electron microscope evidencing H3 hysteresis caused by the tensile strength effect during the gas condensation process and therefore resulted in a monomodal pore-size distribution as obtained from the BJH desorption method.[52,53] Therefore, considering the high surface area and mesoporous characteristics of the WO_3 sample, achieved by dextran addition, was selected for further studies in this manuscript.

To further evaluate the morphology formation of the porous WO_3 sample, the various microstructural analysis was investigated, as shown in Figure 5. During the gel formation, the dextran-added precursor solution creates amorphous networking of the sol as obtained from Figure 5a. The gel collapses into particles that precipitate from the solution during the hydrothermal treatment. This may look like the precursor solution is getting embedded inside the dextran polymeric network. On the other hand, Figure 5b,c exhibit the SEM images of the synthesized WO_3 sample at different magnifications, respectively. The morphology exhibits as the hierarchical platelet-type shapes as obtained by the hydrothermal synthesis. Besides, the TEM bright-field images further reveal that the platelet-type morphology contains a wide range of size of 80−300 nm, having a predominate order of large distinct porosity (Figure 5d,e). The lattice fringes in high-resolution TEM (HRTEM) image (Figure 5f) corresponds to the (020) reflection with an inter planner spacing of 0.379 nm, which confirms the single-crystalline nature of the monoclinic WO_3 phase. The EDS analysis was also performed to confirm the elements of WO_3 and the complete removal of Na, as shown in Figure S1.

X-ray Photoemission Spectroscopic and Photoluminescence Analysis. The valence states of the fundamental elements W and O of the synthesized mesoporous WO_3 have been identified through XPS measurements (Figure 6). The survey spectrum of the WO_3 is shown in Figure 6a. First, two characteristic peaks at 36.0 ± 0.2 eV (Figure 6b) has been ascribed to the typical doublet of W^{6+} with the binding energy of W ($4f_{7/2}$ and $4f_{5/2}$). The peak ratio of W ($4f_{7/2}$) to W ($4f_{5/2}$) was found to be 4:3 with a spin−orbit splitting of a doublet value of 2.12 eV. A third broad peak of W ($5p_{3/2}$) locates at ∼41.8 eV. This result reveals only W for its +6 oxidation state.[54] However, the asymmetry of the W $4f_{7/2}$ indicates that WO_3 readily becomes oxygen-deficient to form WO_{3-x}, with the variable oxygen composition parameter x. On deconvolution, the asymmetric O 1s XPS spectrum evolves into two components centered at 529.21 (O1) and 530.65 eV (O2) as shown in Figure 6c. The dominant O1 component is a characteristic of O^{2-} ions, whereas the O2 component at the higher binding side may be associated with the presence of chemisorbed oxygen in the grain boundaries or the existence of the hydroxyl group (−OH) because of the adsorption of water onto the surface of the WO_3 during synthesis through the aqueous medium route. This oxygen deficiency greatly

https://dx.doi.org/10.1021/acs.jpca.0c02912
J. Phys. Chem. A 2020, 124, 5709−5719

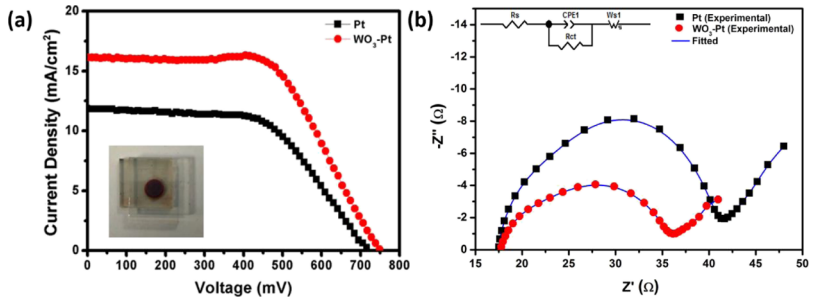

Figure 7. (a) $J-V$ characteristic and (b) corresponding Nyquist plot (inset: corresponding equivalent circuit) for Pt and WO_3−Pt-based DSSC devices, respectively.

Table 1. PV and Impedance Spectroscopic Parameters for Different DSSC Devices

cell	J_{SC} (mA cm^{-2})	V_{OC} (mV)	FF	PCE ± 0.05 (%)	R_S (Ω cm^{-2})	R_{CT1} (Ω cm^{-2})	C_p (F)
without WO_3	11.49	722	0.59	5.01	18.52	32.68	1.52×10^{-6}
Pt−WO_3 (nonporous)	14.68	753	0.55	6.12	18.65	26.86	3.57×10^{-4}
Pt−WO_3 (mesoporous)	16.55	753	0.64	7.43	18.23	27.12	2.48×10^{-3}

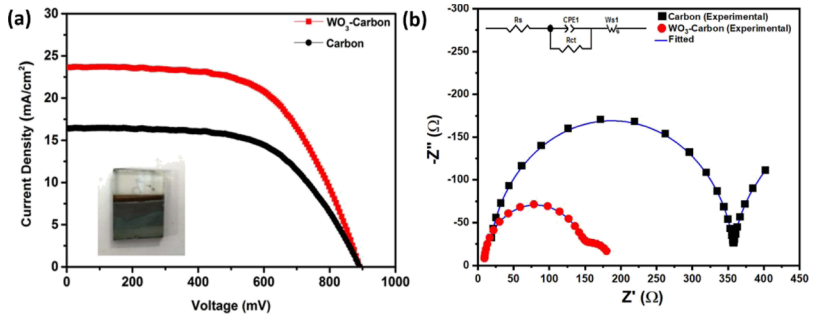

Figure 8. (a) $J-V$ characteristic and (b) corresponding Nyquist plot (inset: corresponding equivalent circuit) for carbon and WO_3−carbon-based PSC devices, respectively.

influences the bulk of the electronic transport properties by introducing donor electronic states.[55]

Further, the photoluminescence (PL) spectrum of the aqueous dispersion of the WO_3 sample was monitored at room temperature, as shown in Figure S3. A blue emission at 467 nm was observed against an excitation wavelength of 350 nm. It is anticipated that the reason for the visible emission exhibited by WO_3 could be due to the presence of oxygen-related defects as observed from the XPS analysis. The aqueous solution of synthesized WO_3 resulted in a quantum yield (QY) of 3.25% at room temperature.

Microstructural and Optical Measurement of WO_3 Films. The SEM line-scale mapping was recorded on the WO_3−Pt film, as shown in Figure S4a. This indicates a homogeneous distribution of W and O throughout the Pt layer. Further, the distribution of W and O over the Pt layer is very clear from the elemental mapping diagram, as shown in Figure S4b. Besides, in the case of WO_3−carbon-based PSC film, a thin layer (<200 nm) of mesoporous WO_3 has been formed as shown in Figure S4c, and the corresponding elemental mapping has been given in Figure S4d. The EDS result indicates that despite the different approach of the buffer layer formation for DSSCs and PSCs, both of them showed a proper distribution of W and O along with their respective back electrode material, indicating that the formulation of WO_3 synthesis is precise and efficient in preparing the well-dispersed sample.

PV Performance of WO_3 as a Cathode Buffer Layer in DSSCs. In order to evaluate the effect of mesoporous WO_3 as a CBL in PV applications, the PV performances have been further investigated. An evaluation of the DSSC performances of the fabricated WO_3-based devices were executed under 1SUN 1.5 AM (Figure 7). The performances of the $J-V$ characteristic plot for the DSSC devices with Pt CE and WO_3−Pt CE are shown in Figure 7a. The WO_3−Pt device exhibited a maximum PCE of 7.43% with a short circuit current (J_{SC}) of 16.25 mA cm^{-2}, an open-circuit voltage (V_{OC}) of 0.75 V, and a fill factor (FF) of 0.59. On the contrary, with only Pt CE-based devices exhibited a PCE of 5.01% with a J_{SC} of 11.49 mA cm^{-2}, a V_{OC} of 0.72 V, and a FF of 0.64. The digital image of WO_3−Pt-based DSSCs has been given in the inset of Figure 7a. The effect of mesoporous nature also influences the efficiency of the device. In the absence of the mesoporous WO_3 layer, the maximum average PCE was achieved to be ∼6.12% (Figure S5a), which is ∼21% lesser than compared to mesoporous WO_3 layer-added devices. These results strongly support the benefits of porous layer incorporation in such a DSSC device. Further, the recorded $J-V$ characteristics parameters are compared in Table 1. In spite of this, using WO_3 on Pt CE, the corresponding device exhibits ∼48% higher efficiency than only Pt CE. The enhancement of PCE was resulted by keeping insignificant alteration in V_{OC} except for the J_{SC} and FF, which signifies the presence of mesoporous WO_3 gets an advantage as a catalyst for Pt CE and, therefore, accelerate the rate of high electron mobility and hole-extraction leading toward high

https://dx.doi.org/10.1021/acs.jpca.0c02912
J. Phys. Chem. A 2020, 124, 5709−5719

Table 2. PV and Impedance Spectroscopic Parameters for Different PSC Devices

cell	J_{SC} (mA cm^{-2})	V_{OC} (mV)	FF	PCE ±0.05 (%)	R_S (Ω cm^{-2})	R_{CT1} (Ω cm^{-2})	C_p (F)
without WO_3	16.82	900	0.59	9.65	32.25	227.3	48.59×10^{-9}
carbon−WO_3 (nonporous)	20.15	891	0.59	10.58	36.92	225.7	32.67×10^{-7}
carbon−WO_3 (mesoporous)	24.21	900	0.60	12.42	20.92	102.2	16.32×10^{-6}

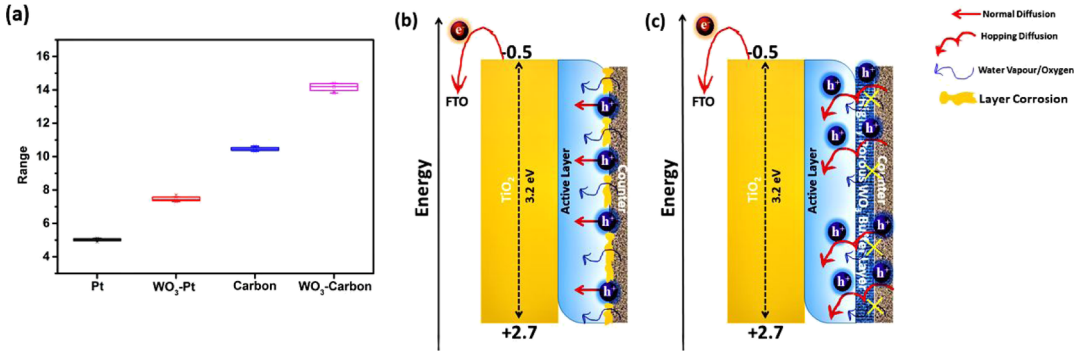

Figure 9. (a) Efficiency measurement error plot for different devices and a schematic representation of (b) in the absence and (c) in the presence of highly porous WO_3 cathode buffer layer for solar cell devices provides some added beneficial features such as hole hopping diffusion, restriction to water vapor/moisture, and less corrosion of the counter electrode.

efficiency. The EIS measurements were carried out to understand the transport properties at different interfaces in the DSSC assembly. The EIS spectra (Nyquist plot) and the corresponding equivalent circuit diagram (inset) of cells for the DSSC devices, as shown in Figure 7b. As shown in Table 1, the DSSCs show almost closure of sheet resistance (R_s), which is due to the use of the same Pt counter electrodes and I^-/I_3^- electrolyte in all the devices. On the other hand, resistance at the Pt/electrolyte interface has been found significantly higher for the only Pt CE device compared to WO_3−Pt-based devices. The CT resistance of 32.68 Ω cm^{-2} at the electrolyte/dye/TiO_2 interface for the Pt CE device is considerably higher than the WO_3−Pt device (27.12 Ω cm^{-2}). This result clearly shows that the catalytic activity of WO_3 reduces the CT resistance of Pt producing higher efficiency. The EIS spectrum of the without mesoporous WO_3-based DSSC device has been given in Figure S5a (inset), and the corresponding data are shown in Table 1.

PV Performance of WO_3 as a Cathode Buffer Layer in PSCs

In addition, incorporation of the synthesized WO_3 as a cathode buffer layer, it was further evaluated in the case of PSC devices. The corresponding J−V characteristics plot is shown in Figure 8a. It was noted that the addition of WO_3−carbon back contact exhibited the highest PCE of 12.42%, which is ∼17 and ∼29% higher than the without mesoporous WO_3 (PCE: ∼10.58%) and only carbon-based devices (∼9.65%), respectively. The J−V characteristics plot for the without mesoporous WO_3-added device has been given in Figure S5b. Interestingly, the V_{OC} does not affect the incorporation of the WO_3 layer, and for both the cases, it shows quite high value as 0.9 V. The addition of WO_3 significantly boosts up the J_{SC} of the WO_3−carbon-based device to 23.16 mA cm^{-2}, which is quite high and impressive to generate higher efficiency. The digital image of the WO_3−carbon-based PSC has been given in the inset of Figure 8a.

The Nyquist plots derived from the impedance data, Figure 8b, revealed a clear difference between the two devices. The WO_3−carbon-based PSC shows the smallest radius of the semicircle in the high-frequency region, which indicates the lowest CT resistance at the $CH_3NH_3PbI_3$/carbon interface. This result implies that the film addition of WO_3 plays an important role in DSSC electron recombination. All the measured parameters have been summarized in Table 2. R_S of PSCs with WO_3 is less than the device without WO_3, which suggests that the hole-extraction process at the carbon electrode with WO_3 is more efficient. Moreover, a lower charge exchange resistances (R_{CT}) at a bias of −0.90 V was observed for WO_3-additive PSCs compared to the devices without additive. However, the WO_3 additive layer may play the role of a hole collector along with the appropriate energy level to the perovskite $CH_3NH_3PbI_3$ sensitizer and lead to an acceleration of the hole extraction efficiency. The WO_3 layer can also significantly reduce the series resistance and significantly improve the J_{SC} of the PSC device. Besides, the EIS measurement was also performed for the absence of mesoporous WO_3-based PSC devices, as shown in Figure S5b (inset), and the corresponding data are summarized in Table 2.

Probable Mechanism of the WO_3 Buffer Layer in Solar Cell Devices. The efficiency was measured for 10 numbers of cells for DSSCs and PSCs with an error bar plot, as shown in Figure 9a. This result implies that the film addition of WO_3 plays an important role in DSSC electron recombination. Therefore, we suggest an apparent mechanism to understand the effect of the porous WO_3 structure as an interfacial cathode buffer layer on the improved crystalline and enhanced PCEs of the solar cell devices. WO_3 treatment may also play a similar role in affecting the electronic structure of carbon and can be explored as a hole-extracting layer for PSCs. It is assumed that a small polaron hopping conduction mechanism can be influenced to operate in WO_3 as a cathode buffer layer for solar cell devices.[56] This mechanism possibly suggests hopping can be a faster way compared to the traditional way of hole diffusion with an extremely fast rate constant that leads to exhibit enhanced device performance. Besides, the photoluminescence spectrum of WO_3 predicts partial oxygen vacancies in substoichiometric WO_{3-x} which creates localized defect states: W^{4+} or W^{5+} and W^{6+}. These mixed valance states may further promote the CT and enhance electrical conductivity.[57,58] The high surface area facilitates to collect and regenerate a higher number of holes, which is ultimately

https://dx.doi.org/10.1021/acs.jpca.0c02912
J. Phys. Chem. A 2020, 124, 5709−5719

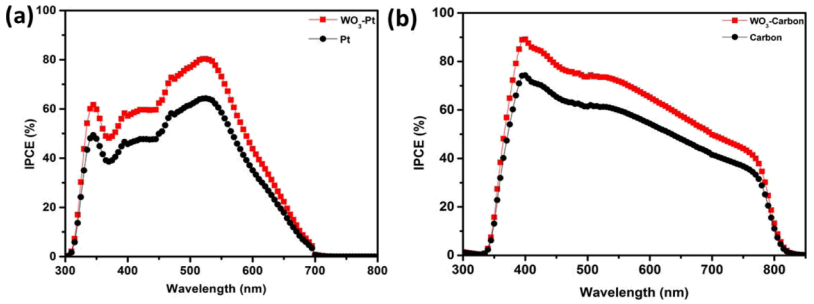

Figure 10. IPCE spectra for (a) WO_3−Pt and Pt-based DSSC and (b) WO_3−carbon- and carbon-based PSC devices, respectively.

beneficial for rapid and smooth electron−hole mobility for the devices. At the same time, it is also assumed that because of distinct porous nature of WO_3, that it may be suitable to entrap/adsorb any moisture or oxygen molecule, which may retard the overall performance of the device. Pt counter electrodes are usually affected by high corrosion because of the use of liquid I^-/I_3^- electrolyte, which can retard the hole conduction process, although using the WO_3 buffer layer may restrict the rate of the corrosion and facilitate the hole conduction process for the device. Therefore, the high porosity could be beneficial for the WO_3 and favor as a buffer layer for the solar cell devices. The overall concept has been schematically illustrated in Figure 9b,c. The enhanced PCE has been mainly influenced by the enhancement of the J_{SC} factor of the device. The increased J_{SC} of the porous WO_3 probably resulted in a thicker active layer, which is helpful to improve optical-trapping properties.

Incident Photon to Current Conversion Efficiency Measurements. IPCE stands for the external quantum efficiency of the DSSC and PSC devices including the effects of optical losses caused by transmission and reflection.[37] The IPCE measurements were also performed as a function of wavelength by comparing the WO_3−Pt and Pt-based devices for DSSCs and WO_3−carbon and carbon-based devices for PSCs as shown in Figure 10. The IPCE curve for all the DSSCs shows a broad peak over the range of 300−800 nm with a maximum value of ∼83% at 536 nm for the WO_3−Pt-based device, whereas the Pt-based DSSC exhibits an IPCE value of 61% at the same wavelength as shown in Figure 10a. In the case of PSCs, incorporation of the WO_3 layer exhibits predominant incident photon to current conversion efficiency (IPCE) value (∼90% at 400 nm and 76% at 560 nm wavelength) than the without WO_3 layer device value (∼76% at 400 nm and 60% at 560 nm wavelength) as shown in Figure 10b. This also strongly recommends that the incorporation of a WO_3 layer improves the IPCE in a great manner to minimize the electron recombination or electron entrapment within surface trap states or electron loss within the hole transporting section of the device.

Therefore, the EIS and IPCE results predict that the CT process is taking place at the interface of Pt/carbon and WO_3, leading to an acceleration of the hole mobility, and as a result, the short circuit current increases remarkably. This is quite competitive with organic interfacial materials where it cannot be readily achieved with the later. All the above-discussed results and the fundamental insights could be useful in the development of achieving solution-processed successful incorporation of the WO_3 cathode buffer layer for high-efficiency devices.[20,28,59] Although the use of WO_3 presented here are far from being fully optimized, but the profound advantages along with ease of preparation and applicability for potential performance make it a good candidate for the cathode buffer layer for solar cell devices.[60,61] This work also provides insights into the design of the interfacial hole transport layer for the fabrication of solution-processed solar cell devices. The obtained results are quite encouraging and open up ample scope to develop new and economically viable synthetic approaches to enhance the performance of the solution-processed solar cell devices.

In spite of this, there are very few reports available on the buffer layer-incorporated DSSC and PSC devices. In comparison to the reported results on the performance of various materials as incorporated buffer layer in solar cell devices (Table 3), the results obtained in this work are quite competitive and interesting to execute dextran template mesoporous WO_3 as a promising buffer layer candidate for both DSSC and PSC devices, respectively.

Table 3. Reported Performances of Different Buffer Layer Used for Various Types of Solar Cells

CBL	type of solar cell[a]	PCE (%)	reference
PAMPS-Na nonconjugated polymer/Al	OSC	9.16	22
PCBM/bis-C_{60}/Ag	PSC	15.44	23
C_{60}/bis-C_{60}/Ag	PSC	13.37	23
TiO_2/Pt	DSSC	2.84	24
CdSe QDs/LiF/AuAg	inverted-PSC	15.1	27
SnO_2/Ag	inverted-OSC	2.89	30
MoO_x/Au	all inorganic PSC	5.52	31
ZnO-DOL/Ag	ISC	3.48	62
Zr-isopropoxide/Al	BHJ-PSC	8.07	63
PCBB-2CN-2C_8/Au	PSC	17.35	64
a-ZrAcac/Al	poly-SC	8.75	65
PCBM, C_{60}, and LiF/Al	planar-PSC	14.69	66
ZnO/PEI/Al	OSC, PSC	11.76	67
ZnO/Ag	OSC	9.2	68
tris-(8-hydroxyquinoline)/Al	planar-PSC	14.22	69
PCBDANI/LiF_2/Al	planar-PSC	15.71	70
bathocuproine/Ag	inverted OSC	3.28	71
PCMP/BCP/Ag	planar PSC	14.47	72
Julolidine	inverted OSC	8.07	73
mesoporous WO_3/Pt	DSSC	7.43	current work
mesoporous WO_3/carbon	mesoscopic PSC	12.42	

[a]OSC: organic solar cells; PSC: perovskite solar cells; DSSC: dye-sensitized solar cells; poly-SC: polymer solar cells; ISC: inverted solar cell; BJH: bulk-hetero junction.

https://dx.doi.org/10.1021/acs.jpca.0c02912
J. Phys. Chem. A 2020, 124, 5709−5719

In our previous report, different concentrations of commercial WO_3 nanoparticles as a HTM incorporated in carbon counter electrodes were tested for PSCs.[35] However, the current study mainly signifies about the mesoporous layer involvement of WO_3 as a CBL for both the DSSC and PSC devices. Of course, controlled synthesis, optimum pore size distribution, various surface treatments, and optimization of film fabrication and device fabrication techniques are required, which may further lead to the enhancement of efficiency of the device for futuristic applications. We believe this study seems to be applicable for the synthesis of other related materials with controllable morphology and tunable textural properties for various applications such as catalysis, adsorption, gas sensing, separation, and so forth.[42−45,48,51]

CONCLUSIONS

Hydrothermal synthesis of mesoporous WO_3 using the dextran templating process has been performed in this study. Dextran can effectively help to generate pore on the surface of WO_3. Hierarchical platelet-like porous morphology of WO_3 exhibited a high surface area of ∼110 m^2 g^{-1} and an average monomodal pore size diameter of 20 nm. Taking advantage of this mesoporous WO_3, it has been further explored as a solution-processed cathode buffer layer on Pt in the case of DSSCs and on carbon for the PSC device performance evaluation. Incorporation of WO_3 interestingly enhanced the PCE of a Pt-based DSSC device by ∼48%, whereas in the case of PSCs, the PCE enhancement was recorded ∼29% compared in the absence of buffer layer-employed devices. It is anticipated that the WO_3 layer significantly boosts up the short circuit current of the PV devices, leading to enhance the PCE. Besides, an apparent hole hopping mechanism associated with the porous WO_3 layer structure credit some added benefits for the devices. On the basis of our results, we are able to establish porosity and buffer layer incorporation as an important factor for PV efficiency enhancement for DSSC and PSC devices. Moreover, the outcome from this work is highly promising and renders a potential for future self-powered electrochromic device integration, where WO_3 will enhance the power generation and switching color in a tandem structure concomitantly.

ASSOCIATED CONTENT

Supporting Information

The Supporting Information is available free of charge at https://pubs.acs.org/doi/10.1021/acs.jpca.0c02912.

Reported surface area and porosity results of different morphology-based WO_3 for various applications; EDS spectrum of the mesoporous WO_3 sample; pore size distribution plot of WO_3 as obtained from the BJH adsorption model; PL spectrum of the aqueous solution of the mesoporous WO_3 sample at room temperature; SEM elemental and line scale mapping of WO_3−Pt and WO_3−carbon films; and J−V characteristics plot along with corresponding fitted EIS plot of the nonporous (without dextran added) WO_3 buffer layer for DSSC and PSC devices (PDF)

AUTHOR INFORMATION

Corresponding Author

Aritra Ghosh − *Environment and Sustainability Institute, University of Exeter, Cornwall TR10 9FE, U.K.;* orcid.org/0000-0001-9409-7592; Email: a.ghosh@exeter.ac.uk

Authors

Anurag Roy − *Environment and Sustainability Institute, University of Exeter, Cornwall TR10 9FE, U.K.;* orcid.org/0000-0002-2097-9442

Shubhranshu Bhandari − *Environment and Sustainability Institute, University of Exeter, Cornwall TR10 9FE, U.K.*

Senthilarasu Sundaram − *Environment and Sustainability Institute, University of Exeter, Cornwall TR10 9FE, U.K.*

Tapas K. Mallick − *Environment and Sustainability Institute, University of Exeter, Cornwall TR10 9FE, U.K.*

Complete contact information is available at: https://pubs.acs.org/10.1021/acs.jpca.0c02912

Notes

The authors declare no competing financial interest.

In support of open access research, all underlying article materials can be accessed upon request via email to the corresponding author.

ACKNOWLEDGMENTS

This work is partly funded by the EPSRC funded JUICE project (EP/P003605/1). The project's funders were not directly involved in the writing of this article. Besides, S.B. would like to acknowledge the College of Engineering, Mathematics and Physical Sciences, the University of Exeter for the PhD fellowship. This work was also supported by the EPSRC_IAA (UK) fund (grant no: EP/R511699/1) obtained by Dr Aritra Ghosh.

REFERENCES

(1) Nayak, P. K.; Mahesh, S.; Snaith, H. J.; Cahen, D. Photovoltaic Solar Cell Technologies: Analyzing the State of the Art. *Nat. Rev. Mater.* **2019**, *4*, 269−285.

(2) Luceño-Sánchez, J.; Díez-Pascual, A.; Peña Capilla, R. Materials for Photovoltaics: State of Art and Recent Developments. *Int. J. Mol. Sci.* **2019**, *20*, 976.

(3) Li, J.; Wong, W.-Y.; Tao, X.-m. Recent Advances in Soft Functional Materials: Preparation, Functions and Applications. *Nanoscale* **2020**, *12*, 1281−1306.

(4) Wright, M.; Uddin, A. Organic-Inorganic Hybrid Solar cells: A Comparative Review. *Sol. Energy Mater Sol.* **2012**, *107*, 87−111.

(5) Grätzel, M. Dye-Sensitized Solar Cells. *J. Photochem. Photobiol., C* **2003**, *4*, 145−153.

(6) Karim, N. A.; Mehmood, U.; Zahid, H. F.; Asif, T. Nanostructured Photoanode and Counter Electrode Materials for Efficient Dye-Sensitized Solar Cells (DSSCs). *Sol. Energy* **2019**, *185*, 165−188.

(7) Park, N. G. Research Direction toward Scalable, Stable, and High Efficiency Perovskite Solar Cells. *Adv. Energy Mater.* **2020**, *10*, 1903106.

(8) Gao, X. X.; Luo, W.; Zhang, Y.; Hu, R.; Zhang, B.; Züttel, A.; Feng, Y.; Nazeeruddin, M. K. Stable and High-Efficiency Methylammonium-Free Perovskite Solar Cells. *Adv. Mater.* **2020**, *32*, 1−9.

(9) Jena, A. K.; Kulkarni, A.; Miyasaka, T. Halide Perovskite Photovoltaics: Background, Status, and Future Prospects. *Chem. Rev.* **2019**, *119*, 3036−3103.

(10) Yeoh, M.-E.; Chan, K.-Y. Recent Advances in Photo-Anode for Dye-Sensitized Solar Cells: A Review. *Int. J. Energy Res.* **2017**, *41*, 2446−2467.

(11) Kouhnavard, M.; Ikeda, S.; Ludin, N. A.; Ahmad Khairudin, N. B.; Ghaffari, B. V.; Mat-Teridi, M. A.; Ibrahim, M. A.; Sepeai, S.; Sopian, K. A Review of Semiconductor Materials as Sensitizers for Quantum Dot-Sensitized Solar Cells. *Renew. Sust. Energ. Rev.* **2014**, *37*, 397−407.

(12) Lee, C.-P.; Li, C.-T.; Ho, K.-C. Use of Organic Materials in Dye-Sensitized Solar Cells. *Mater. Today* **2017**, *20*, 267−283.

(13) Mahmood, A. Recent Research Progress on Quasi-solid-state Electrolytes for Dye-Sensitized Solar Cells. *J. Energy Chem.* **2015**, *24*, 686−692.
(14) Zhou, Z.; Pang, S. Highly Efficient Inverted Hole-Transport-Layer-Free Perovskite Solar Cells. *J. Mater. Chem. A* **2020**, *8*, 503−512.
(15) Jung, H. S.; Han, G. S.; Park, N.-G.; Ko, M. J. Flexible Perovskite Solar Cells. *Joule* **2019**, *3*, 1850−1880.
(16) Deepak, T. G.; Anjusree, G. S.; Thomas, S.; Arun, T. A.; Nair, S. V.; Sreekumaran Nair, A. A Review on Materials for Light Scattering in Dye-Sensitized Solar Cells. *RSC Adv.* **2014**, *4*, 17615−17638.
(17) Li, D.; Ågren, H.; Chen, G. Near Infrared Harvesting Dye-Sensitized Solar Cells Enabled by Rare-Earth Upconversion Materials. *Dalton Trans.* **2018**, *47*, 8526−8537.
(18) Park, N.-G.; Zhu, K. Scalable Fabrication and Coating Methods for Perovskite Solar Cells and Solar Modules. *Nat. Rev. Mater.* **2020**, *5*, 333−350.
(19) Qi, B.; Zhang, Z.; Wang, J. Uncovering the Role of Cathode Buffer Layer in Organic Solar Cells. *Sci. Rep.* **2015**, *5*, 7803.
(20) Tan, Z. a.; Li, L.; Cui, C.; Ding, Y.; Xu, Q.; Li, S.; Qian, D.; Li, Y. Solution-Processed Tungsten Oxide as an Effective Anode Buffer Layer for High-Performance Polymer Solar Cells. *J. Phys. Chem. C* **2012**, *116*, 18626−18632.
(21) Po, R.; Carbonera, C.; Bernardi, A.; Camaioni, N. The Role of Buffer Layers in Polymer Solar Cells. *Energy Environ. Sci.* **2011**, *4*, 285−310.
(22) Cai, Y.; Chang, L.; You, L.; Fan, B.; Liu, H.; Sun, Y. Novel Nonconjugated Polymer as Cathode Buffer Layer for Efficient Organic Solar Cells. *ACS Appl. Mater. Interfaces* **2018**, *10*, 24082−24089.
(23) Liang, P.-W.; Chueh, C.-C.; Williams, S. T.; Jen, A. K.-Y. Roles of Fullerene-Based Interlayers in Enhancing the Performance of Organometal Perovskite Thin-Film Solar Cells. *Adv. Energy Mater.* **2015**, *5*, 1402321.
(24) Lungu, J.; Socol, G.; Stan, G. E.; Ştefan, N.; et al. Pulsed Laser Fabrication of TiO_2 Buffer Layers for Dye Sensitized Solar Cells. *Nanomaterials* **2019**, *9*, 746.
(25) Luculescu, J. Y.; Kim, S. H.; Lee, H.-H.; Lee, K.; Ma, W.; Gong, X.; Heeger, A. J. New Architecture for High-Efficiency Polymer Photovoltaic Cells using Solution-Based Titanium Oxide as an Optical Spacer. *Adv. Mater.* **2006**, *18*, 572.
(26) Hayakawa, A.; Yoshikawa, O.; Fujieda, T.; Uehara, K.; Yoshikawa, S. High Performance Polythiophene/Fullerene Bulk-Heterojunction Solar Cell with a TiO_x Hole Blocking Layer. *Appl. Phys. Lett.* **2007**, *90*, 163517.
(27) Tan, F.; Xu, W.; Hu, X.; Yu, P.; Zhang, W. Highly Efficient Inverted Perovskite Solar Cells with CdSe QDs/LiF Electron Transporting Layer. *Nanoscale Res. Lett.* **2017**, *12*, 614.
(28) Liang, Z.; Zhang, Q.; Jiang, L.; Cao, G. ZnO Cathode Buffer Layers for Inverted Polymer Solar Cells. *Energy Environ. Sci.* **2015**, *8*, 3442−3476.
(29) Rajbhandari, P. P.; Dhakal, T. P. Low Temperature ALD Growth Optimization of ZnO, TiO_2, and Al_2O_3 to be used as a Buffer Layer in Perovskite Solar Cells. *J. Vac. Sci. Technol., A* **2020**, *38*, 032406.
(30) Tran, V.-H.; Ambade, R. B.; Ambade, S. B.; Lee, S.-H.; Lee, I.-H. Low-Temperature Solution-Processed SnO_2 Nanoparticles as a Cathode Buffer Layer for Inverted Organic Solar Cells. *ACS Appl. Mater. Interfaces* **2017**, *9*, 1645−1653.
(31) Liu, C.; Li, W.; Chen, J.; Fan, J.; Maia, Y.; Schropp, R. E. I. Ultra-thin MoO_x as Cathode Buffer Layer for the Improvement of All-Inorganic $CsPbIBr_2$ Perovskite Solar Cells. *Nano Energy* **2017**, *41*, 75−83.
(32) Oh, W. C.; Cho, K. Y.; Jung, C. H.; et al. Hybrid of Graphene Based on Quaternary $Cu_2ZnNiSe_4$ -WO_3 Nanorods for Counter Electrode in Dye-Sensitized Solar Cell Application. *Sci. Rep.* **2020**, *10*, 4738.
(33) Ni, M.; Leung, M. K. H.; Leung, D. Y. C.; Sumathy, K. An Analytical Study of the Porosity Effect on Dye-Sensitized Solar Cell Performance. *Sol. Energy Mater Sol.* **2006**, *90*, 1331−1344.
(34) Zheng, H.; Tachibana, Y.; Kalantar-zadeh, K. Dye-Sensitized Solar Cells Based on WO_3. *Langmuir* **2010**, *26*, 19148−19152.
(35) Bhandari, S.; Roy, A.; Ghosh, A.; Mallick, T. K.; Sundaram, S. Performance of WO_3-Incorporated Carbon Electrodes for Ambient Mesoscopic Perovskite Solar Cells. *ACS Omega* **2020**, *5*, 422−429.
(36) Moon, J.; Shin, W.; Park, J. T.; Jang, H. Solid-State Solar Energy Conversion from WO_3 Nano and Microstructures with Charge Transportation and Light-Scattering Characteristics. *Nanomaterials* **2019**, *9*, 1797.
(37) Roy, A.; Das, P. P.; Selvaraj, P.; Sundaram, S.; Devi, P. S. Perforated $BaSnO_3$ Nanorods Exhibiting Enhanced Efficiency in Dye Sensitized Solar Cells. *ACS Sustain. Chem. Eng.* **2018**, *6*, 3299−3310.
(38) Selvaraj, P.; Roy, A.; Ullah, H.; Sujatha Devi, P.; Tahir, A. A.; Mallick, T. K.; Sundaram, S. Soft-Template Synthesis of High Surface Area Mesoporous Titanium Dioxide for Dye-Sensitized Solar Cells. *Int. J. Energy Res.* **2019**, *43*, 523−534.
(39) Pecquenard, B.; Lecacheux, H.; Livage, J.; Julien, C. Orthorhombic WO_3 Formed *via* a Ti-Stabilized WO_3.1/3 H_2O Phase. *J. Solid State Chem.* **1998**, *135*, 159−168.
(40) Thummavichai, K.; Wang, N.; Xu, F.; Rance, G.; Xia, Y.; Zhu, Y. *In situ* Investigations of the Phase Change Behaviour of Tungsten Oxide Nanostructures. *R. Soc. Open Sci.* **2018**, *5*, 171932.
(41) Thommes, M.; Kaneko, K.; Neimark, A. V.; et al. Physisorption of Gases with Special Reference to the Evaluation of Surface Area and Pore Size Distribution (IUPAC Technical Report). *Pure Appl. Chem.* **2015**, *87*, 1051−1069.
(42) Olivier, H.; Gao, J.; Li, M.; Zhao, Y.; et al. Mesoporous WO_3 Nanofibers with Crystalline Framework for High-Performance Acetone Sensing. *Front. Chem.* **2019**, *7*, 1−11.
(43) Mei, L.; Zhao, H.; Lu, B. Ultra-efficient Photocatalytic Properties in Porous Tungsten Oxide/Graphene Film under Visible Light Irradiation. *Adv. Sci.* **2015**, *2*, 1500116.
(44) Lu, Z.; Kanan, S. M.; Tripp, C. P. Synthesis of High Surface Area Monoclinic WO_3 Particles using Organic Ligands and Emulsion Based Methods. *J. Mater. Chem.* **2002**, *12*, 983−989.
(45) Yang, J.; Zhang, X.; Liu, H.; Wang, C.; et al. Heterostructured TiO2/WO3 porous microspheres: Preparation, characterization and photocatalytic properties. *Catalysis Today* **2013**, *201*, 195−202.
(46) Wei, S.; Zhao, G.; Du, W.; Tian, Q. Synthesis and Excellent Acetone Sensing Properties Of Porous WO_3 Nanofibers. *Vacuum* **2016**, *124*, 32−39.
(47) Huang, J.; Xu, X.; Gu, C.; Fu, G.; Wang, W.; Liu, J. Flower-Like and Hollow Sphere-Like WO_3 Porous Nanostructures: Selective Synthesis and Their Photocatalysis Property. *Mater. Res. Bull.* **2012**, *47*, 3224−3232.
(48) Zhang, J.; Tu, J.-p.; Du, G.-h.; Dong, Z.-m.; Su, Q.-m.; Xie, D.; Wang, X.-l. Pt Supported Self-Assembled Nest-Like-Porous WO_3 Hierarchical Microspheres as Electrocatalyst for Methanol Oxidation. *Electrochim. Acta* **2013**, *88*, 107−111.
(49) Nandiyanto, A. B. D.; Arutanti, O.; Ogi, T.; Iskandar, F.; Kim, T. O.; Okuyama, K. Synthesis of Spherical Macroporous WO_3 Particles and Their High Photocatalytic Performance. *Chem. Eng. Sci.* **2013**, *101*, 523−532.
(50) Hara, K.; Zhao, Z.-G.; Cui, Y.; Miyauchi, M.; Miyashita, M.; Mori, S. Nanocrystalline Electrodes Based on Nanoporous-Walled WO_3 Nanotubes for Organic-Dye-Sensitized Solar Cells. *Langmuir* **2011**, *27*, 12730−12736.
(51) Zhang, H.; Wang, J.; Liu, X.; Ma, X.; Zhu, W. Hydrothermal Synthesis of Pure-Phase Hierarchical Porous Hexagonal WO_3 Microspheres as Highly Efficient Support for Pd Catalyst for Hydrogenation. *Particuology* **2018**, *41*, 126−132.
(52) Ghosh, S.; Das, R.; Naskar, M. K. Morphologically tuned Aluminum Hydrous Oxides and Their Calcined Products. *J. Am. Ceram. Soc.* **2016**, *99*, 2273−2282.
(53) Vinogradov, V. V.; Agafonov, A. V.; Vinogradov, A. V.; Gulyaeva, T. I.; Drozdov, V. A.; Likholobov, V. A. Sol-gel Synthesis,

https://dx.doi.org/10.1021/acs.jpca.0c02912
J. Phys. Chem. A 2020, 124, 5709−5719

Characterization and Catalytic Activity of Mesoporous C-Alumina Prepared from Boehmite Sol by Different Methods. *J. Sol. Gel Sci. Technol.* **2010**, *56*, 333−339.
(54) Ji, R.; Zheng, D.; Zhou, C.; Cheng, J.; Yu, J.; Li, L. Low-Temperature Preparation of Tungsten Oxide Anode Buffer Layer *via* Ultrasonic Spray Pyrolysis Method for Large-Area Organic Solar Cells. *Materials* **2017**, *10*, 820.
(55) Chatten, R.; Chadwick, A. V.; Rougier, A.; Lindan, P. J. D. The Oxygen Vacancy in Crystal Phases of WO_3. *J. Phys. Chem. B* **2005**, *109*, 3146−3156.
(56) Vemuri, R. S.; Bharathi, K. K.; Gullapalli, S. K.; Ramana, C. V. Effect of Structure and Size on The Electrical Properties of Nanocrystalline WO_3 films. *ACS Appl. Mater. Interfaces* **2010**, *2*, 2623−2628.
(57) Gillet, M.; Lemire, C.; Gillet, E.; Aguir, K. The Role of Surface Oxygen Vacancies upon WO_3 Conductivity. *Surf. Sci.* **2003**, *532−535*, 519−525.
(58) Granqvist, C. G. Electrochromic Tungsten Oxide Films: Review of Progress 1993-1998. *Sol. Energy Mater. Solar Cells* **2000**, *60*, 201−262.
(59) Qiu, M.; Zhu, D.; Bao, X.; Wang, J.; Wang, X.; Yang, R. WO3 with surface oxygen vacancies as an anode buffer layer for high performance polymer solar cells. *J. Mater. Chem. A* **2016**, *4*, 894−900.
(60) Pitchaiya, S.; Natarajan, M.; Santhanam, A.; Asokan, V.; et al. A Review on the Classification of Organic/Inorganic/Carbonaceous Hole Transporting Materials for Perovskite Solar Cell Application. *Arabian J. Chem.* **2020**, *13*, 2526−2557.
(61) Yuvapragasam, L.; Zhang, S.; Yang, S.; Li, X.; Yu, Y.; Wei, Q.; Ni, Z.; Li, M. Influence of Hole Transport Material/Metal Contact Interface on Perovskite Solar Cells. *Nanotechnology* **2018**, *29*, 255201.
(62) Samavati, A.; Samavati, Z.; Ismail, A. F.; Othman, M. H. D.; Rahman, M. A.; Amiri, I. S. Effect of Organic Ligand-Decorated ZnO Nanoparticles as a Cathode Buffer Layer on Electricity Conversion Efficiency of an Inverted Solar Cell. *RSC Adv.* **2018**, *8*, 1418−1426.
(63) Luo, Z.; Yang, B.; Bai, Y.; Hayat, T.; Alsaedi, A.; Tan, Z. a. Efficient Polymer Solar Cells with Alcohol-Soluble Zirconium(IV) Isopropoxide Cathode Buffer Layer. *Energies* **2018**, *11*, 328.
(64) Li, Y.; Zhao, Y.; Chen, Q.; et al. Multifunctional Fullerene Derivative for Interface Engineering in Perovskite Solar Cells. *J. Am. Chem. Soc.* **2015**, *137*, 15540−15547.
(65) Yang, Z.; Li, S.; Wang, F.; Qian, D.; Lin, J.; Hou, J.; Li, Y. High Performance Polymer Solar Cells with As-Prepared Zirconium Acetylacetonate Film as Cathode Buffer Layer. *Sci. Rep.* **2015**, *4*, 4691.
(66) Liu, X.; Yu, H.; Yan, L.; Dong, Q.; Wan, Q.; Zhou, Y.; Song, B.; Li, Y. Triple Cathode Buffer Layers Composed of PCBM, C_{60}, and LiF for High-Performance Planar Perovskite Solar Cells. *ACS Appl. Mater. Interfaces* **2015**, *7*, 6230−6237.
(67) Jia, X.; Wu, N.; Wei, J.; et al. A Low-Cost and Low-Temperature Processable Zinc oxidepolyethylenimine (ZnO:PEI) Nano-Composite as Cathode Buffer Layer for Organic and Perovskite Solar Cells. *Org. Electron.* **2016**, *38*, 150−157.
(68) Zhang, S.; Gupta, V.; Sharma, C.; Haranath, D.; Kumar, M.; Chand, S. Luminescent Cathode Buffer Layer for Enhanced Power Conversion Efficiency and Stability of Bulk-Heterojunction Solar Cells. *Org. Electron.* **2016**, *38*, 193−199.
(69) Chen, L.; Wang, G.; Niu, L.; Yao, Y.; Guan, Y.; Cui, Y.; Song, Q. High Performance Planar p-i-n Perovskite Solar Cells Based on a Thin Alq3 Cathode Buffer Layer. *RSC Adv.* **2018**, *8*, 15961−15966.
(70) Liu, X.; Huang, P.; Dong, Q.; et al. Enhancement of the Efficiency and Stability of Planar p-i-n Perovskite Solar Cells *via* Incorporation of an Amine-Modified Fullerene Derivative as a Cathode Buffer Layer. *Sci. China Chem.* **2017**, *60*, 136−143.
(71) Wang, F.; Patil, B. R.; Mohtaram, F.; et al. Inverted Organic Solar Cells with Non-Clustering Bathocuproine (BCP) Cathode Interlayers Obtained by Fullerene Doping. *Sci. Rep.* **2019**, *9*, 10422.
(72) He, C.; Zhang, F.; Zhao, X.; Lin, C.; Ye, M. Interface Engineering of BCP Buffer Layers in Planar Heterojunction Perovskite Solar Cells with NiO_x Hole Transporting Layers. *Front. Phys.* **2018**, *6*, 99.
(73) Eom, S. H.; Do, H. J.; Lee, J.; Jung, I. H.; Yoon, S. C.; Lee, C. Interfacial modifier having Julolidine for the Cathode Buffer Layer in PTB-7:PC_{70}BM Based Inverted Organic Photovoltaic Cells. *J. Nanosci. Nanotechnol.* **2018**, *18*, 7037−7042.

https://dx.doi.org/10.1021/acs.jpca.0c02912
J. Phys. Chem. A 2020, 124, 5709−5719